Timothy No
Department of Mechanical, Aerospace, and Biomedical Engineering,
University of Tennessee,
Knoxville, TN 37996
e-mail: tno@vols.utk.edu

Michael Gomez
Department of Mechanical, Aerospace, and Biomedical Engineering,
University of Tennessee,
Knoxville, TN 37996
e-mail: mgomez5@vols.utk.edu

Ryan Copenhaver
Department of Mechanical, Aerospace, and Biomedical Engineering,
University of Tennessee,
Knoxville, TN 37996
e-mail: rcopenh1@vols.utk.edu

Juan Uribe Perez
GOM Americas Inc.,
Charlotte, NC 28223
e-mail: j.uribe@gom.com

Christopher Tyler
The Boeing Company,
Berkeley, MO 63134
e-mail: christopher.tyler@boeing.com

Tony L. Schmitz
Department of Mechanical, Aerospace, and Biomedical Engineering,
University of Tennessee,
Knoxville, TN 37996;
Oak Ridge National Laboratory,
Manufacturing Demonstration Facility,
Knoxville, TN 37932
e-mail: tony.schmitz@utk.edu

Force and Stability Modeling for Non-Standard Edge Geometry Endmills

This paper describes a reverse engineering solution for modeling the behavior of non-standard edge geometry endmills. Structured light scanning is used to produce a solid model of the endmill and spatial coordinates for the points that define the cutting edges that are extracted. These points are then used to determine the cutting edge radius and angle at equally spaced points along the tool's axis. This cutting edge geometry is applied directly in a time domain simulation that predicts the cutting force and tool/workpiece deflection for user-selected operating parameters. A good agreement between predicted and measured cutting forces is first demonstrated for two non-standard edge geometry endmills. Second, the results of stability tests are compared with simulation predictions for multiple spindle speed-axial depth of cut combinations using one of the endmills. The time records are analyzed by periodically sampling the measured and predicted displacement and velocity. Third, the time domain simulation is used to generate a stability map that separately identifies stable (forced vibration) behavior, secondary Hopf bifurcations, and period-n bifurcations. [DOI: 10.1115/1.4045057]

Keywords: milling, dynamics, serrated, force, stability, simulation, fringe projection, machine tool dynamics, machining processes, metrology

1 Introduction

Multi-axis machining is a cornerstone manufacturing capability for discrete part production. Technology improvements are consistently pursued and implemented to increase productivity and efficiency. Examples include the following: new machine designs to increase part access, work volume, acceleration, velocity, stiffness, and accuracy; controller improvements to reduce positioning and contouring errors; new spindle designs to increase power, torque, rotation speed, and thermal stability; new tool holder designs to increase clamping stiffness and reduce runout; and new tool designs to increase stiffness, provide localized cooling/lubrication at the tool/chip interface, control chip formation, and increase material removal rates.

For endmills, design modifications to the cutting teeth include non-uniform spacing (or pitch), variable helix angle from one tooth to the next and along a single cutting edge, edge honing, and serrated edge geometry, among others. The purpose of these design updates is to affect chip formation and disturb the tooth-to-tooth chip thickness regeneration that serves as the mechanism for self-excited vibration, or chatter, in endmilling operations. While modeling of machining operations has received continuous international attention since the mid-twentieth century (see Refs. [1–3] for comprehensive overviews), relatively less effort has been expended on modeling the behavior of these non-standard geometry endmills, particularly those with serrated cutting edges. Notable exceptions are summarized here.

Wang and Yang [4] presented force models in the angle and frequency domains for a cylindrical roughing endmill with sinusoidal cutting edges. Merdol and Altintas [5] modeled the serration profile by fitting points along a cubic spline projected on the helical flutes. This geometric model was used in a time domain milling model. Dombovari et al. [6] used the semi-discretization method to analyze the stability of serrated endmills. Later, he and others created general models for various tool geometries [7,8]. Koca and Budak [9] used a linear edge-force model and the semi-discretization method for force and stability modeling and optimized the serration waveform shape to reduce milling forces and increase stability. Grabowski et al. [10] extended their mechanistic model to calculate the process forces for serrated endmills. Tehranizadeh and Budak [11] proposed a genetic algorithm to optimize the design of serration shapes. Comak and Budak [12] modeled the stability behavior of variable pitch and helix endmills using both a frequency domain solution and the semi-discretization method. Experimental results were compared with the simulations. Munoa et al. [13] summarized chatter suppression techniques, including special tool geometries with discrete time delays (helical, variable pitch, and serrated) and continuous time delays (variable helix

Manuscript received January 25, 2019; final manuscript received September 3, 2019; published online October 2, 2019. Assoc. Editor: Satish Bukkapatnam.

and harmonically varied helix). The work described here builds on these prior efforts by enabling the actual edge coordinates of the endmill under test to be extracted from a structured light scan and implemented directly in a time domain simulation.

As noted, a reverse engineering solution for modeling the behavior of non-standard edge geometry endmills is provided. The procedure include: (1) structured light scanning to produce a solid model of the endmill (this is useful because the tool geometry may not be available from the manufacturer); (2) identification of the spatial coordinates for the points that define the cutting edges; (3) analysis of those points to extract the cutting edge radius and angle at equally spaced slices along the tool axis; (4) time domain simulation of the cutting force and tool/workpiece deflection using the measured edge geometry; and (5) periodic sampling of the simulation outputs to analyze stability.

The paper outline is as follows: In Sec. 2, the structured light scanning approach is described, and the example results are presented. In Sec. 3, the time domain simulation is detailed. In Sec. 4, the experimental setup for milling trials is detailed. In Sec. 5, a comparison between measured and simulated forces is presented for stable cutting conditions over a range of axial depths and feed per tooth values. The results of stability testing and predictions are also provided. In Sec. 6, a process stability map is presented that separately identifies stable (forced vibration) behavior, secondary Hopf bifurcations, and period-n bifurcations. Finally, conclusions are provided in Sec. 7. Primary contributions of this paper are the following: (1) structured light scanning to determine the spatial coordinates of the cutting edges in a reverse engineering strategy; (2) a time domain simulation that uses the measured edge coordinates directly and models variation in the radius of the serrated edge as runout; and (3) the identification of period-n bifurcation behaviour for a selected non-standard geometry endmill.

2 Scanning Metrology for Edge Geometry

A primary challenge associated with modeling the performance of non-standard edge geometry endmills is that the design details are not generally available. To overcome this obstacle, the reverse engineering capabilities made possible by scanning metrology can be leveraged. One strategy for collecting point clouds from complex surfaces to develop the corresponding solid model is structured light, or fringe, projection. In this technique, a common approach is to project a pattern of parallel lines onto the surface in question. The reflected lines are distorted due to the surface geometry. The measurement system uses the relative positions of the projector and one or more cameras (two cameras is typical) together with the distorted lines to reconstruct the three-dimensional surface. While many commercial options are available, the GOM ATOS Capsule system was used for this research.

The measurements are proceeded by first preparing the endmill surface using a removable anti-glare coating and attaching reference targets to the shank surface to enable multiple measurements to be stitched together and generate the solid model; a photograph is provided in Fig. 1. Multiple scans were then completed (Fig. 2) to obtain the point cloud and 3D model (Fig. 3). Mesh details are provided in Fig. 4. Figures 2–5 display results for an endmill from Walter Tools (part number 3D1163-6768616). Figures 6–7 present results for a Niagara endmill (part number N68949).

The procedure used to extract the edge coordinates from the solid model included four steps:

- First, using the best fit cylinder to the tool shank and the fluted end's extreme point, the origin was established on the tool's centerline.
- Second, the points located on the cutting edges were selected. This step required manual manipulation within the GOM software. In function, it was analogous to update the driving directions in Google Maps by dragging the original route to new roads.

Fig. 1 Endmill preparation for structured light scanning: example endmill (left) and application of anti-glare coating and reference targets (right)

- Third, the radius r and angle ϕ for each edge point was calculated. The teeth angles were normalized to a selected tooth and constrained to values between 0 and 360 deg; the z value was retained to obtain a triplet $\{r, \phi, z\}$ for each point.
- Fourth, because the point density was higher than required for the time domain simulation, linear interpolation was used to obtain the triplet for axial slices located every 0.1 mm over the full flute length (see Fig. 8), which shows the origin, edge points, and axial slices for the Walter Tool endmill.

Example radius and angle results for the Walter Tool endmill are provided in Figs. 9 and 10. It is observed in Fig. 9 that the specialized tool geometry incorporates large radius variation along the cutting edge and that these radius variations are phased from one tooth to the next (120 deg spacing between the peaks for the three

Fig. 2 Scanning metrology setup using the GOM ATOS Capsule system

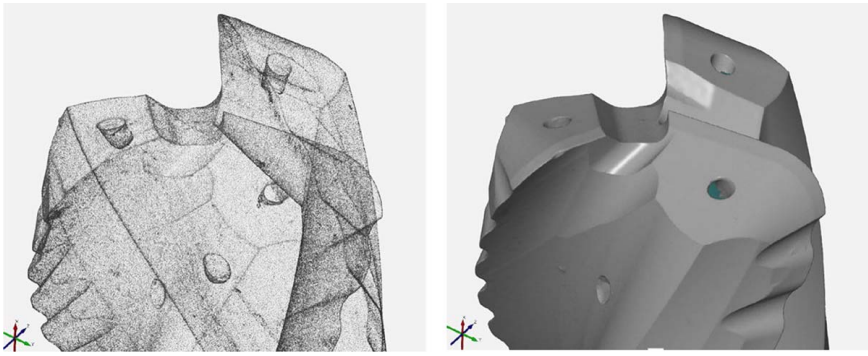

Fig. 3 Point cloud (left) and model (right) for the Walter Tools endmill obtained from scanning

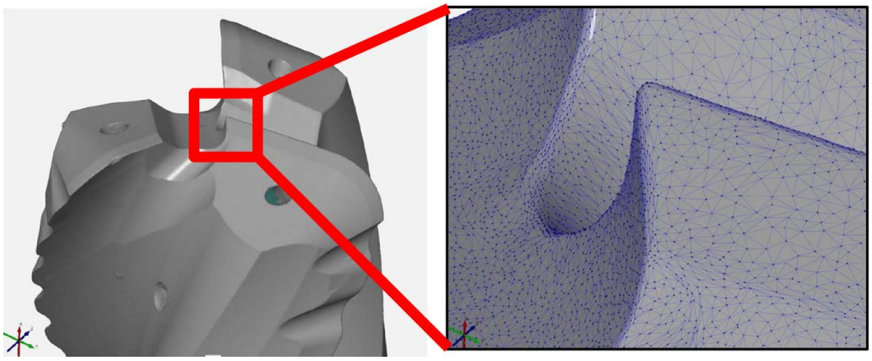

Fig. 4 Model (left) and mesh details (right) for the Walter Tools endmill

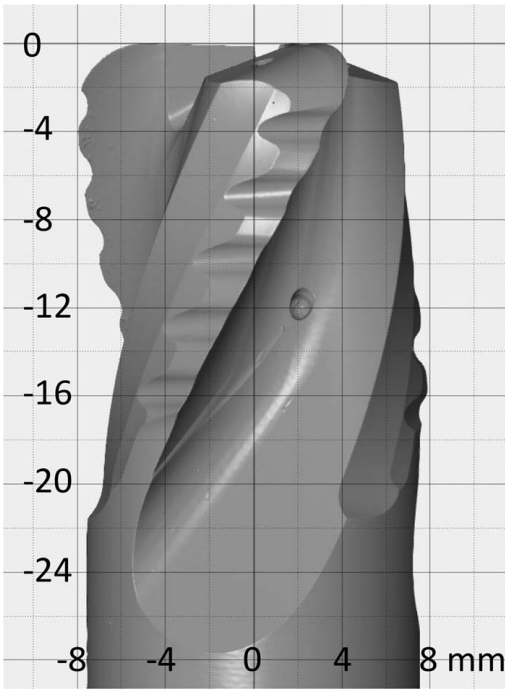

Fig. 5 Scale for the Walter Tool endmill to visualize edge geometry

teeth). In Fig. 10, it is seen that the angle variation from the nominal helix $\Delta\phi$ is not significant. The mechanism for increased stability with this design is, therefore, the segmentation of the cutting edge into bands using the radius variation. This effectively reduces the axial depth of cut on each tooth, while simultaneously increasing the thickness of the chip. The tooth-dependent axial depth is smaller than the commanded axial depth because the large radius variation causes only a portion of the helical length to be engaged in the cut at an instant in time. Also, the point cloud data were used to determine the macro-geometry: 8 mm shank radius, 28.3 deg helix angle, and 2.785 mm bull nose radius.

Due to the manual manipulation in the second step, it was desired to determine the sensitivity of the cutting edge coordinate identification and, by extension, the radius and angle values used in the time domain simulation. To assess this sensitivity, the manual manipulation used to identify the cutting edges was performed five times for each edge (15 total data sets) for a single tool scan of the Walter Tool endmill. This isolated the contribution of the edge identification from potential non-repeatability in the scan (this uncertainty was not evaluated in this study). The standard deviations in the radius, $\sigma(r)$, and angle, $\sigma(\phi)$, are displayed in Figs. 11 and 12. It is seen that the deviations are small, and the data are therefore sufficient to make meaningful process performance predictions when incorporated in the time domain simulation. For example, the standard deviation in radius is approximately 5 μm on average. This is only 1% of the overall radius variation (480 μm).

Example radius and angle results for the Niagara endmill are provided in Figs. 13 and 14. It is observed in Fig. 13 that there is no appreciable radius variation in this case. Figure 14 shows that the angle variation is periodic and progressively offset by 90 deg between teeth (harmonically varied helix). The mechanism for increased stability with this design is, therefore, disruption of regeneration from one tooth to the next by the periodically variable cutting edge angle on each tooth and the offset from one edge to the next. The point cloud data were again used to determine the macro-geometry: 9.5 mm shank radius and 35.1 deg helix angle.

3 Time Domain Simulation

Time domain simulation enables the numerical solution of the coupled, time-delay equations of motion for milling in small time steps [1]. It is well suited to incorporating the inherent complexities

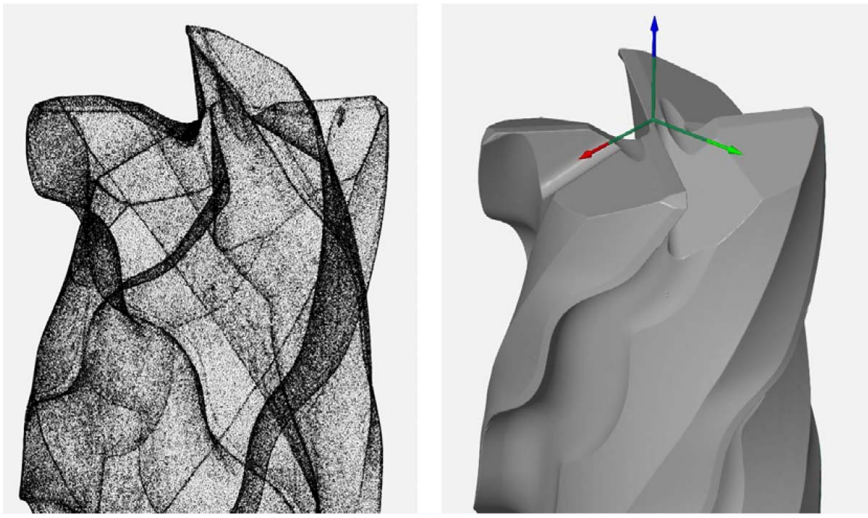

Fig. 6 Point cloud (left) and model (right) for the Niagara endmill

of milling dynamics, including complicated tool geometries (runout, or different radii, of the cutter teeth, non-uniform teeth spacing, and variable helix) and the nonlinearity that occurs if the tooth leaves the cut due to large magnitude vibrations. The simulation applied here is based on the regenerative force, dynamic deflection model described by Smith and Tlusty [14]. As opposed to analytical or semi-analytical stability maps that provide a global picture of the stability behavior, time domain simulation provides information regarding the local cutting force and vibration behavior for the selected cutting conditions. The simulation used in this study is described in the following paragraphs.

The strategy used to model the large radius variation for each tooth on the Walter Tool endmill (Fig. 9) was to define a nominal tooth shape with no serration and then incorporate the radial deviation as runout. It is observed in Fig. 15 that tooth 3 follows the nominal bull nose profile up to the shank diameter. The tooth 3 geometry was therefore selected as the reference (up to −2.4 mm). The radius was set to a constant value of 7.974 mm (i.e., the value at −2.4 mm) for z values of −2.5 mm and beyond. The runout was then determined for each tooth as the difference between the reference profile and the actual radius value at each z interval. The runout, RO, is displayed in Fig. 16. The peak-to-peak variation is approximately 0.48 mm. For the Niagara endmill, the runout was small, but the intentional z-dependent variation in edge angle and, therefore, the tooth spacing (or pitch) was incorporated by specifying the tooth angle at each z location using the interpolated data from the 3D model edge identification.

The time domain simulation had three special requirements for the selected tools: use the actual tooth angles, include the radius variation as runout, and incorporate the bull nose geometry. For the tooth angles, the measured angles from the scanned edge were arranged in an array, where the columns were the individual teeth and the rows were the z locations (in steps of 0.1 mm). These z locations extended over the entire cutting length, but the array was

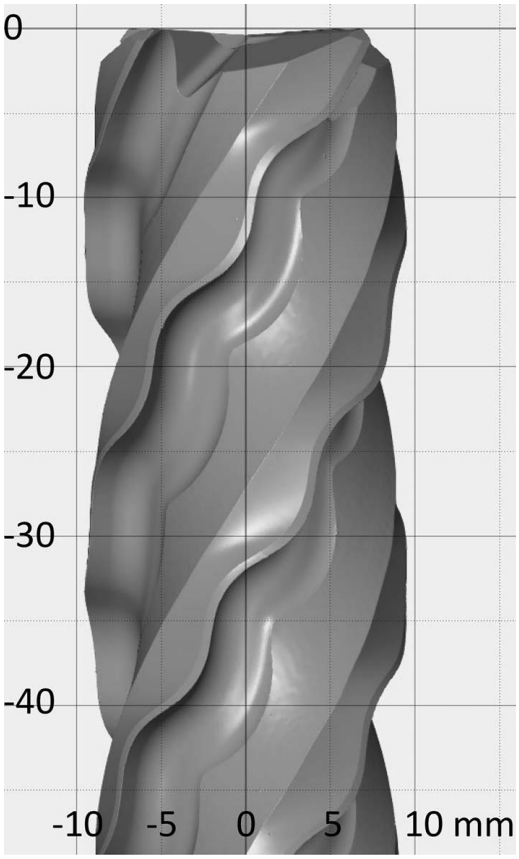

Fig. 7 Scale for the Niagara 3D model to visualize edge geometry

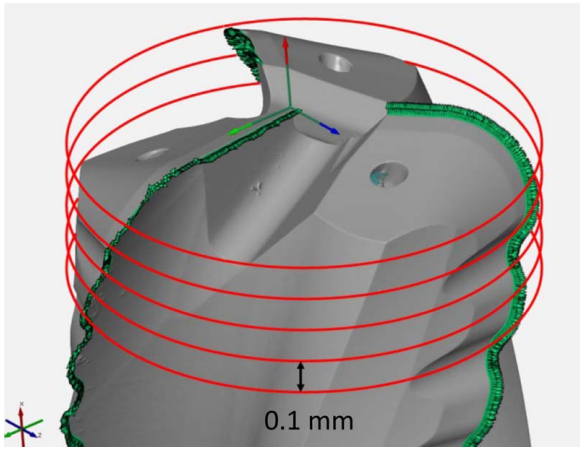

Fig. 8 Cutting edge points and axial slices (not to scale) for linear interpolation. The origin is also identified (Walter Tool).

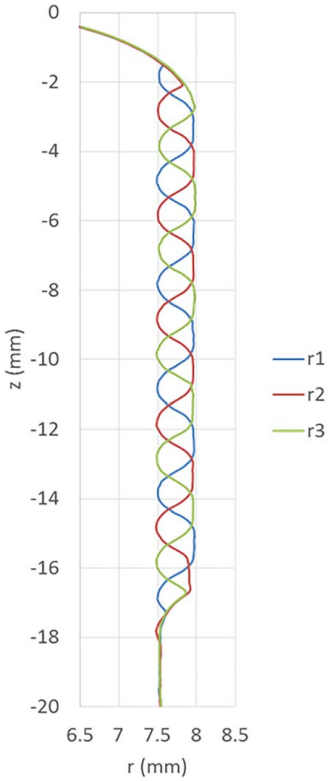

Fig. 9 Radius value at each axial slice for all three endmill teeth (Walter Tool)

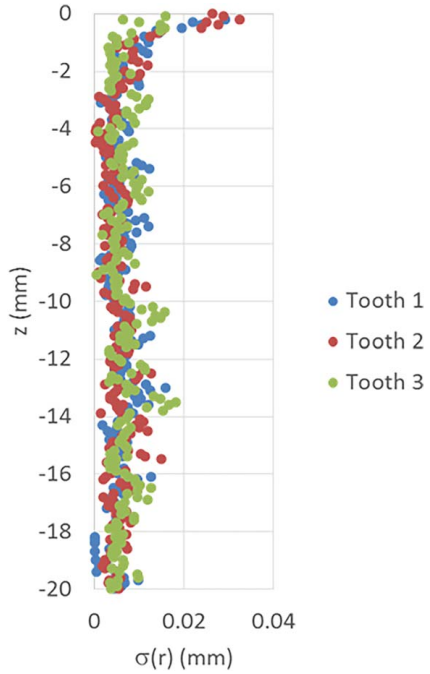

Fig. 11 Standard deviations in the radius, $\sigma(r)$, from the manual edge identification step (Walter Tool)

truncated to include rows only up to the commanded axial depth when the simulation was executed. This enables any axial depth to be simulated (up to the cutting length). A row array of closely spaced tooth angles for use in the time domain simulation was then defined. The resolution in this array was $\Delta\phi = 360/SR$, where SR is the number of steps per revolution in the simulation.

Once this array was defined, the measured tooth angles were specified in an index array with each entry given by the ratio $\phi/\Delta\phi$ rounded to the nearest integer, where ϕ is the measured angle of the tooth at the selected z location. This index array was

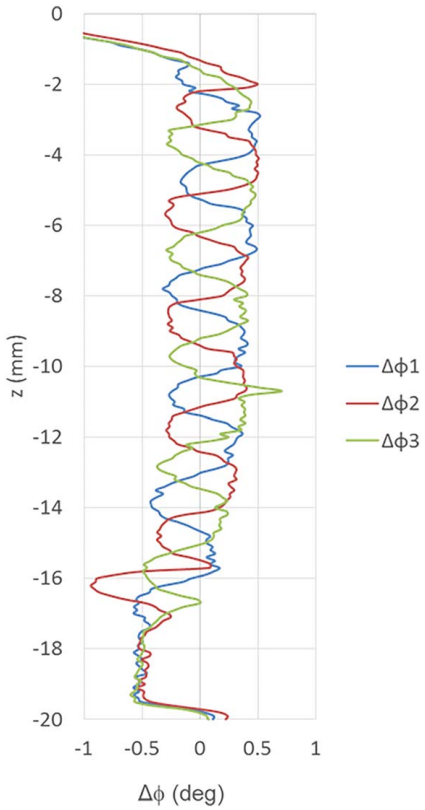

Fig. 10 Deviations of teeth angles from nominal helix (Walter Tool)

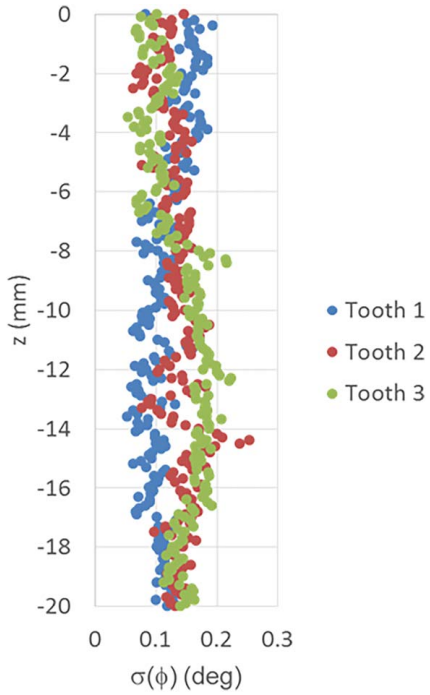

Fig. 12 Standard deviations in the teeth angles, $\sigma(\phi)$, from the manual edge identification step (Walter Tool)

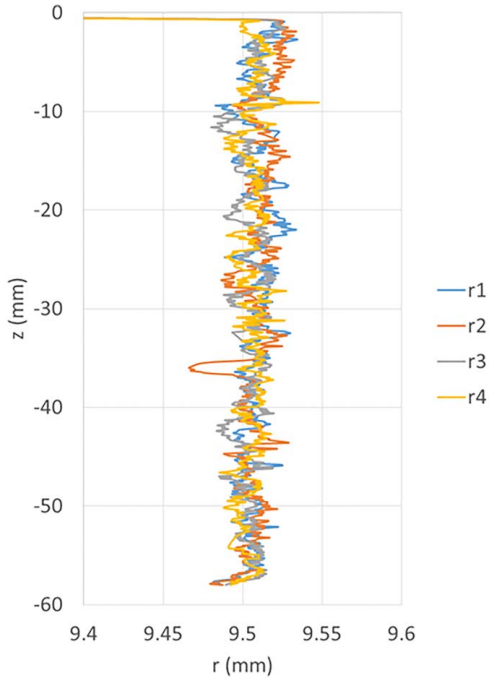

Fig. 13 Radius value at each axial slice for all four endmill teeth (Niagara)

then used to specify the angle of any tooth at any z location by identifying the nearest preselected value from the closely spaced tooth angle array for use in the simulation. The reason for this approach is that the current chip thickness in milling depends not only on the commanded chip thickness and current vibration but also on the surface left by the previous teeth at the current tooth angle. To be able to do so conveniently, this information must be organized according to specified tooth angles.

The tool's radius variation was included as the runout, as noted. The z-dependent *RO* values for each tooth were also arranged in an array, where the columns were the individual teeth and the rows were the z locations (again in steps of 0.1 mm). Note that the *RO* values are negative as shown in Fig. 11. A negative *RO* value

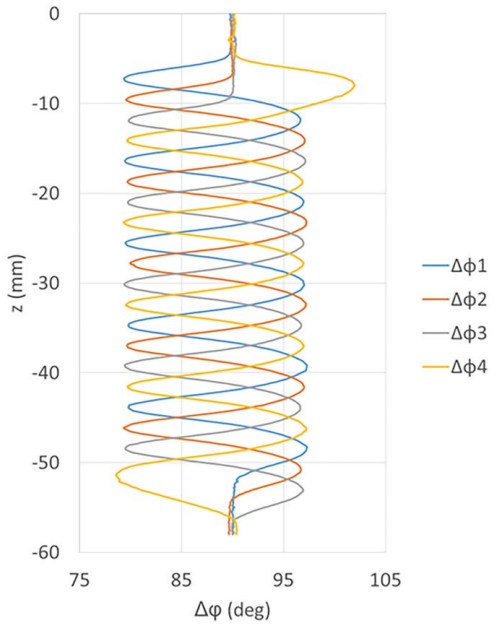

Fig. 14 Deviations of teeth angles from nominal helix (Niagara)

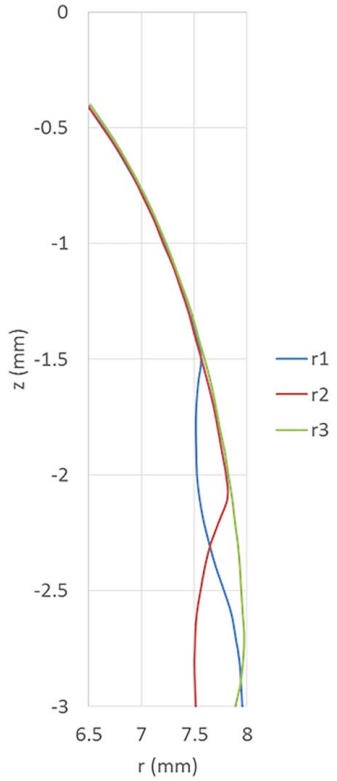

Fig. 15 Selection of tooth 3 as the reference tooth shape (Walter Tool)

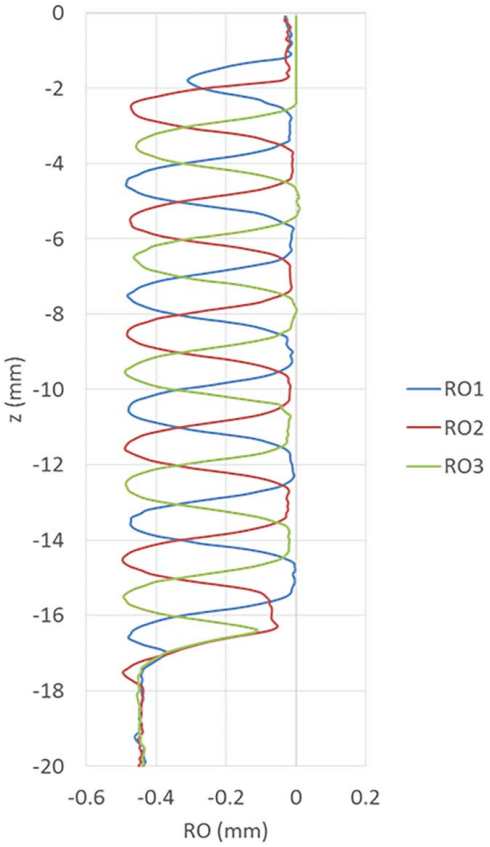

Fig. 16 Runout, *RO*, for three teeth used in time domain simulation. The peak-to-peak variation is approximately 0.48 mm (Walter Tool).

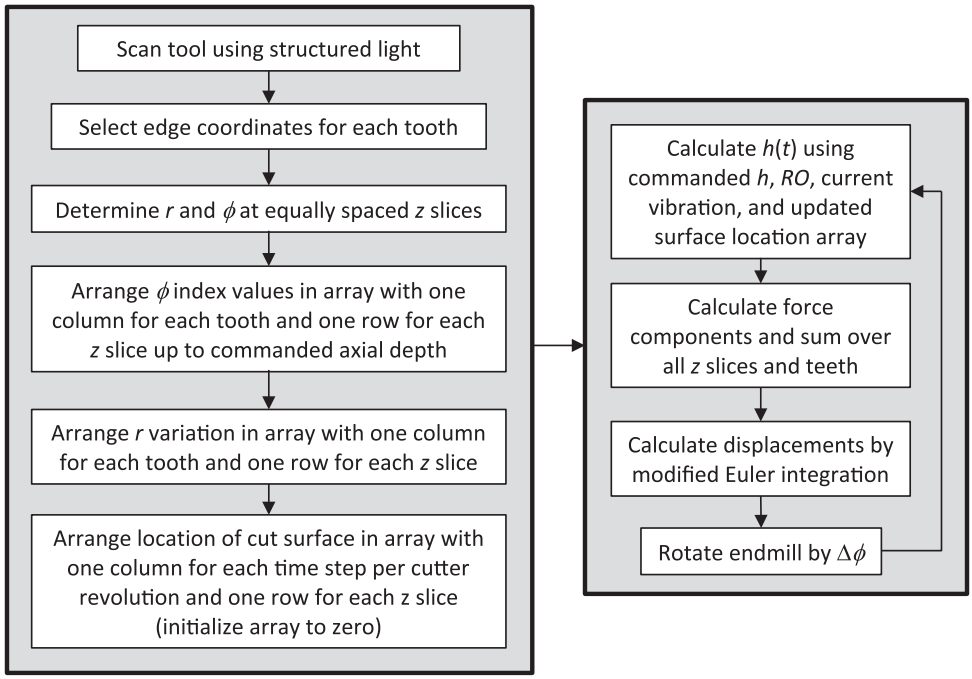

Fig. 17 Time domain simulation flowchart: setup information (left) and simulation steps (right)

reduces the chip thickness for the current tooth but leaves behind material that the next tooth must remove (and therefore increases that chip thickness).

Two other data organization requirements were (1) the surface that was left behind by the current tooth; and (2) the commanded chip thickness. To keep track of the previously machined surface, another array was defined that recorded the surface location in the tool's normal direction for each simulation time step. The columns of this matrix were the number of steps per revolution, and the rows were the z locations. The influence of runout on subsequent chip thickness values was captured in this matrix. Because there were variations in the tooth angles from the nominal helix profile, the commanded chip thickness was also modified to account for the actual tooth angle using the circular tooth path approximation. This approximation calculates the nominal chip thickness from the product of the feed per tooth and the sine of the tooth angle. Finally, the bullnose portion of the Walter Tool endmill was incorporated in the simulation by projecting the forces in the appropriate directions using the nose surface normal at each z location. Also, the axial depth was updated to account for the nose radius arc length [1].

Given this information, the simulation proceeded as follows:

(1) The instantaneous chip thickness $h(t)$ was determined using the commanded chip thickness, runout, and vibration of the current and previous teeth at the selected tooth angle.
(2) The cutting force components in the tangential t and normal n directions were calculated at each axial slice using the following equation:

$$F_t(t) = k_{tc} b h(t) + k_{te} b \tag{1}$$

$$F_n(t) = k_{nc} b h(t) + k_{ne} b \tag{2}$$

where b is the slice width (0.1 mm) and the cutting force coefficients are identified by the subscripts: t or n for direction, and c or e for cutting or edge effect. These forces were then summed over all axial slices engaged in the cut.
(3) The summed force components were used to find the new displacements by numerical solution of the differential equations of motion in the x (feed) and y directions:

$$m_x \ddot{x} + c_x \dot{x} + k_x x = F_t(t)\cos + F_n(t)\sin \tag{3}$$

$$m_y \ddot{y} + c_y \dot{y} + k_y y = F_t(t)\sin - F_n(t)\cos \tag{4}$$

where m is the modal mass, c is the modal viscous damping coefficient, and k is the modal stiffness. The subscripts identify the direction and multiple degrees-of-freedom in each direction can be accommodated by summing the modal contributions.
(4) The tool rotation angle was incremented by adding one to each entry in the tooth angle index array, and the process was repeated.

A flowchart is provided in Fig. 17 to summarize the simulation steps.

4 Experimental Setup

The experimental setup for milling force measurement is shown in Fig. 18. Trials were completed on a Haas TM-1 three-axis computer numerically controlled milling machine. The 7075 aluminum workpiece was mounted on a cutting force dynamometer (Kistler 9257B), and the endmill was clamped in a collet holder and inserted in the CAT-40 spindle interface. For the Walter Tool endmill, tests were performed at axial depths of cut from 4 mm to 14 mm. The commanded feed per tooth for these down (climb) milling experiments was 75 μm/tooth, the spindle speed was 4000 rpm, and the radial depth of cut was 2 mm (12.5% of radial immersion). In a second set of tests, the axial depth was held constant at 8 mm and the feed per tooth was varied from 25 μm/tooth to 100 μm/tooth. The same spindle speed and radial depth were used. The tool and workpiece frequency response functions (FRFs) were measured by impact testing, where an instrumented hammer is used to excite the structure and the response is measured using a linear transducer (a low-mass accelerometer for this research). The results are presented in Fig. 19. Modal fitting was applied to extract the modal parameters for the time domain simulation (Table 1).

For the Niagara endmill, tests were performed at axial depths of cut from 5 mm to 25 mm. The commanded feed per tooth for these

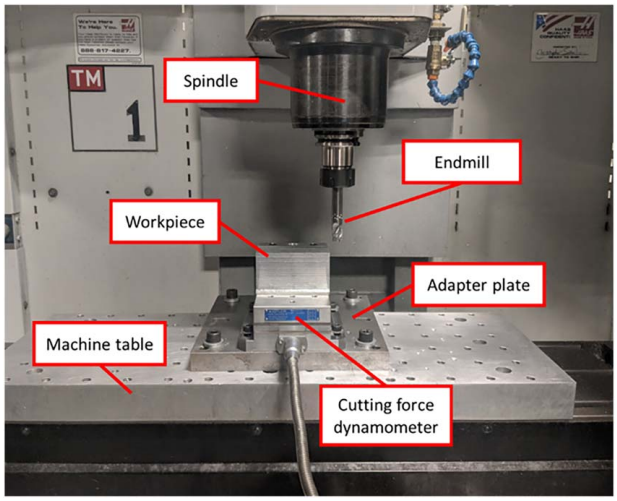

Fig. 18 Experimental setup for milling force measurement

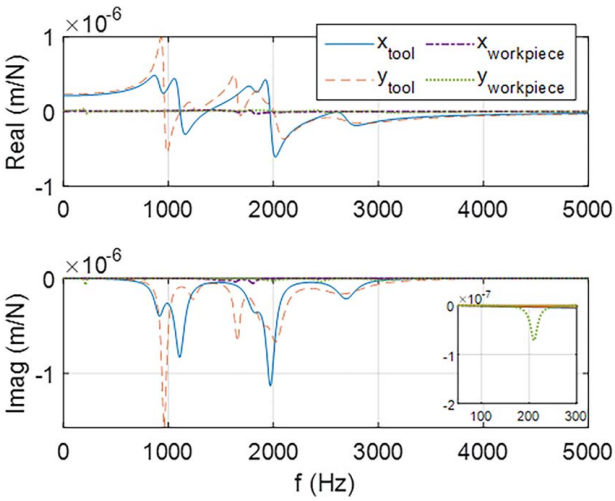

Fig. 19 FRFs of tool and workpiece for the force measurement setup (Walter Tool)

down (climb) milling experiments was 100 μm/tooth, the spindle speed was 3000 rpm, and the radial depth of cut was 1.9 mm (10% radial immersion). The FRF was again measured, and the modal parameters were extracted for use in the time domain simulation (Table 2).

The setup for the Walter Tool endmill stability testing was similar to that shown in Fig. 18, but the aluminum alloy workpiece was mounted on a parallelogram, leaf-type flexure rather than the dynamometer (the flexible direction for the flexure was oriented parallel with the machine's x direction) (Fig. 20). The modal parameters are listed in Table 3; note that the workpiece (flexure) x direction is significantly more flexible than the tool or flexure y direction.

The cutting force coefficients for the 7075 aluminum alloy workpiece were $k_{tc} = 1150$ N/mm^2, $k_{nc} = 522$ N/mm^2, $k_{te} = 25$ N/mm, and $k_{ne} = 25$ N/mm. The same values were used for all predictions.

5 Results

5.1 Force Prediction and Measurement for Walter Tool Endmill. Measured and predicted feed direction force values, F_x, for $b = \{4, 8, 12, \text{and } 14\}$ mm are shown in Fig. 21. A good agreement is observed in all cases. It is seen that the force progresses from a smoother profile while engaged in the cut for $b = 4$ mm to highly discontinuous at $b = 14$ mm. This is the result of the tool design which cuts with approximately 1 mm wide "bands" of limited axial depth, where the local radius is close to the shank diameter. These bands are separated on each cutting edge by the

Table 1 Modal parameters for force measurement setup (Walter Tool)

Direction	m (kg)	k (N/m)	c (N s/m)
Tool			
x	0.756	2.50×10^7	522
x	0.257	1.25×10^7	179
x	0.381	4.95×10^7	348
x	0.120	1.85×10^7	75
x	0.209	6.00×10^7	283
y	0.294	1.07×10^7	105
y	1.101	6.65×10^7	106
y	0.392	4.25×10^7	684
y	27.77	4.00×10^7	162
y	0.140	2.27×10^7	2670
y	0.118	3.33×10^7	142
Workpiece			
x	0.373	3.37×10^7	496
x	1.039	1.10×10^8	363
x	0.466	6.00×10^7	180
x	0.019	1.12×10^7	232
y	95.58	1.67×10^8	10,610
y	73.65	1.77×10^9	12,280
y	21.05	2.03×10^9	7856
y	2.780	4.32×10^8	3258
y	3.203	7.67×10^8	1983
y	1.616	5.87×10^8	2279

Table 2 Modal parameters for force measurement setup (Niagara)

Direction	m (kg)	k (N/m)	c (N s/m)
Tool			
x	20.12	4.08×10^7	4628
x	58.95	5.00×10^8	8584
x	1.208	4.00×10^7	625
x	0.288	1.45×10^7	143
x	0.881	7.25×10^7	799
x	0.799	1.00×10^8	322
x	0.822	1.10×10^8	323
x	0.081	1.30×10^7	41
x	0.088	2.50×10^7	163
x	0.322	1.89×10^8	436
y	23.38	1.03×10^8	4544
y	0.250	9.47×10^6	103
y	3.081	1.70×10^8	1373
y	1.454	9.45×10^7	703
y	6.842	5.50×10^8	2454
y	0.470	5.20×10^7	163
y	0.151	2.25×10^7	74
y	0.147	2.50×10^7	77
y	0.080	2.25×10^7	188
y	0.306	1.75×10^8	413
Workpiece			
x	1.988	9.54×10^7	1360
x	8.833	1.62×10^9	24,737
y	76.84	1.38×10^8	13,037
y	317.78	2.15×10^9	33,393
y	89.063	2.29×10^9	21,316
y	49.18	2.39×10^9	63,493
y	11.51	8.08×10^8	13,928
y	5.532	8.02×10^8	4183
y	8.512	4.87×10^9	9040
y	91.50	6.19×10^{10}	39,507

Table 3 Modal parameters for stability testing setup (Walter Tool)

Direction	m (kg)	k (N/m)	c (N s/m)
Tool			
x	0.593	2.01×10^7	416
x	0.328	1.50×10^7	222
x	0.095	1.44×10^7	94
x	0.124	3.50×10^7	333
y	0.325	1.20×10^7	119
y	0.784	5.00×10^7	889
y	0.550	6.00×10^7	228
y	0.338	5.00×10^7	247
y	0.210	3.50×10^7	130
y	0.176	5.10×10^7	394
Workpiece			
x	2.976	1.74×10^6	93
y	79.06	2.50×10^7	1067
y	52.48	1.12×10^8	13,800
y	214.84	1.32×10^9	21,301
y	17.03	2.44×10^8	5285
y	2.958	7.07×10^7	1215

approximately 2.5 mm spatial period (or wavelength) of the radius variation along the tooth helix (see Figs. 5 and 9). As the axial depth increases, more bands are individually engaged (with a larger than commanded chip thickness) and the force is subsequently increasingly discontinuous even though all cuts are stable (forced vibration only).

Figure 22 displays measured and predicted F_x results for feed per tooth values of {25, 50, 75, and 100} μm/tooth. While the force levels grow with the increased chip thickness, they do not become as increasingly discontinuous as the results presented in Fig. 21. This is because the axial depth was fixed at 8 mm for these tests.

5.2 Force Prediction and Measurement for Niagara Endmill. Measured and predicted feed direction force values for $b = \{5, 15, 20, \text{and } 25\}$ mm are shown in Fig. 23. As shown in Figs. 7 and 14, the spatial period (or wavelength) for the pitch angle variation is approximately 10 mm. This means that 2.5 mm periods were engaged for the highest axial depth. The force profile progresses from a typical down milling signal for $b = 5$, where the pitch angle variation is not fully incorporated, to nearly constant at $b = 20$ mm, where two full spatial periods are engaged.

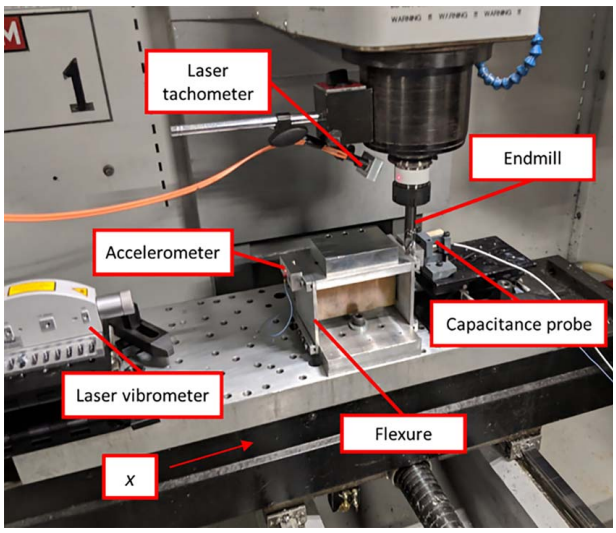

Fig. 20 Experimental setup for stability testing

5.3 Stability Prediction and Validation for Walter Tool Endmill. Given the validated force results, stability testing was completed using the setup depicted in Fig. 20. Workpiece (flexure) displacement and velocity predictions were generated using the time domain simulation, where the system dynamics are provided in Table 3. Note that the natural frequency for the flexure's x direction changed slightly (small fractions of a Hertz level) after each cut because the material was removed from the workpiece. The FRF was measured after each test cut and the actual modal parameters were used in the time domain simulation for predicting the process behavior. The down milling radial depth of cut was 3 mm, and the commanded feed per tooth was 100 μm/tooth for all tests.

To establish stability, the workpiece x direction displacement and velocity signals were sampled once per revolution (i.e., at the spindle rotating frequency) [15,16]. The laser tachometer as shown in Fig. 20 was used to generate the sampling signal. This periodic sampling approach was used to determine if the milling response was synchronous with the spindle rotation (or not) by constructing Poincaré maps (i.e., the periodically sampled displacement was plotted versus the periodically sampled velocity) for both experiment and prediction. To interpret these Poincaré maps, if the cut is stable (i.e., it exhibits forced vibration only), the data repeats with each spindle revolution and the sampled points appear at one location. If self-excited vibration (i.e., regenerative chatter or secondary Hopf bifurcation) occurs, however, an elliptical distribution of sampled points is observed due to the presence of both the (generally) incommensurate chatter frequency and the tooth passing frequency (and its harmonics). Additionally, period-n bifurcations can occur, where n represents the number of periods between repetition. A period-3 bifurcation, for example, exhibits motion that repeats every three rotations. Results are presented in Figs. 24–26 for three spindle speed-axial depth combinations, where the once-per-revolution samples (circles) are superimposed on the continuous x direction workpiece displacement x_w and velocity dx/dt_w. A good agreement is observed overall with three different behaviors represented. Disagreements in scale can be attributed to uncertainties in the structural dynamics and force model.

6 Stability Map

Given the validated time domain simulation for the measured edge geometry, a stability map was next generated to summarize the process behavior over a range of spindle speeds and axial depths of cut for the Walter Tool endmill. For the system dynamics, the mean natural frequency from all test cuts was selected for the workpiece x direction. All other structural dynamics were obtained from Table 3. The down milling radial depth of cut was 3 mm, and the commanded feed per tooth was 100 μm/tooth. For the stability map, simulations were completed at spindle speeds from 2400 rpm to 4000 rpm (10 rpm steps) and axial depths from 0.1 mm to 10 mm (0.1 mm steps).

The stability behavior was automatically determined by synchronous sampling. As described previously, stable behavior can be identified from the distribution of periodically sampled points. If the points repeat each revolution, then only forced vibration is present and the cut is stable. If they do not repeat, then either secondary Hopf or period-n bifurcations are present. To distinguish between the alternatives automatically and qualitatively, the metrics described in Refs. [15,16] were employed. In this case, however, the sampling was completed once-per-spindle revolution rather than with each tooth period. This is because the tooth profiles differed for the three teeth on the selected endmill, and therefore, the behavior does not repeat from tooth-to-tooth, even under stable cutting conditions.

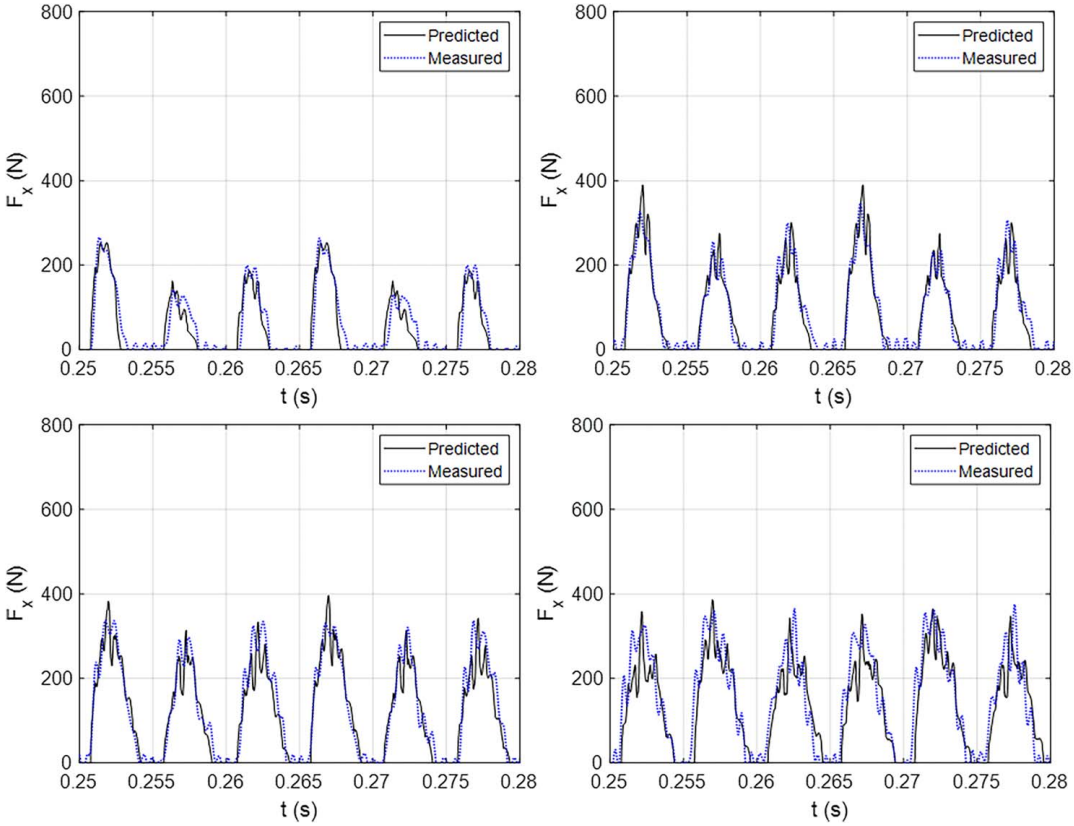

Fig. 21 Measured and predicted force for $b = 4$ mm (top-left), 8 mm (top-right), 12 mm (bottom-left), and 14 mm (top-right)

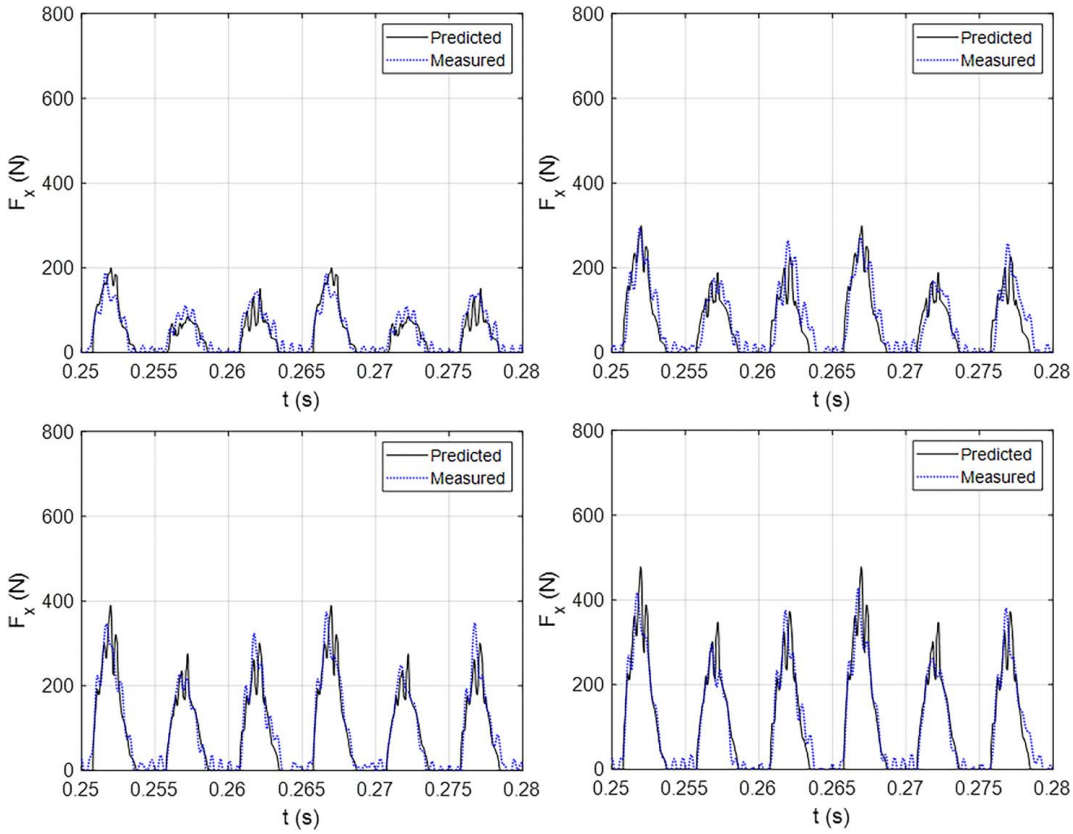

Fig. 22 Measured and predicted force for $f_t = 25$ μm/tooth (top-left), 50 μm/tooth (top-right), 75 μm/tooth (bottom-left), and 100 μm/tooth (bottom-right)

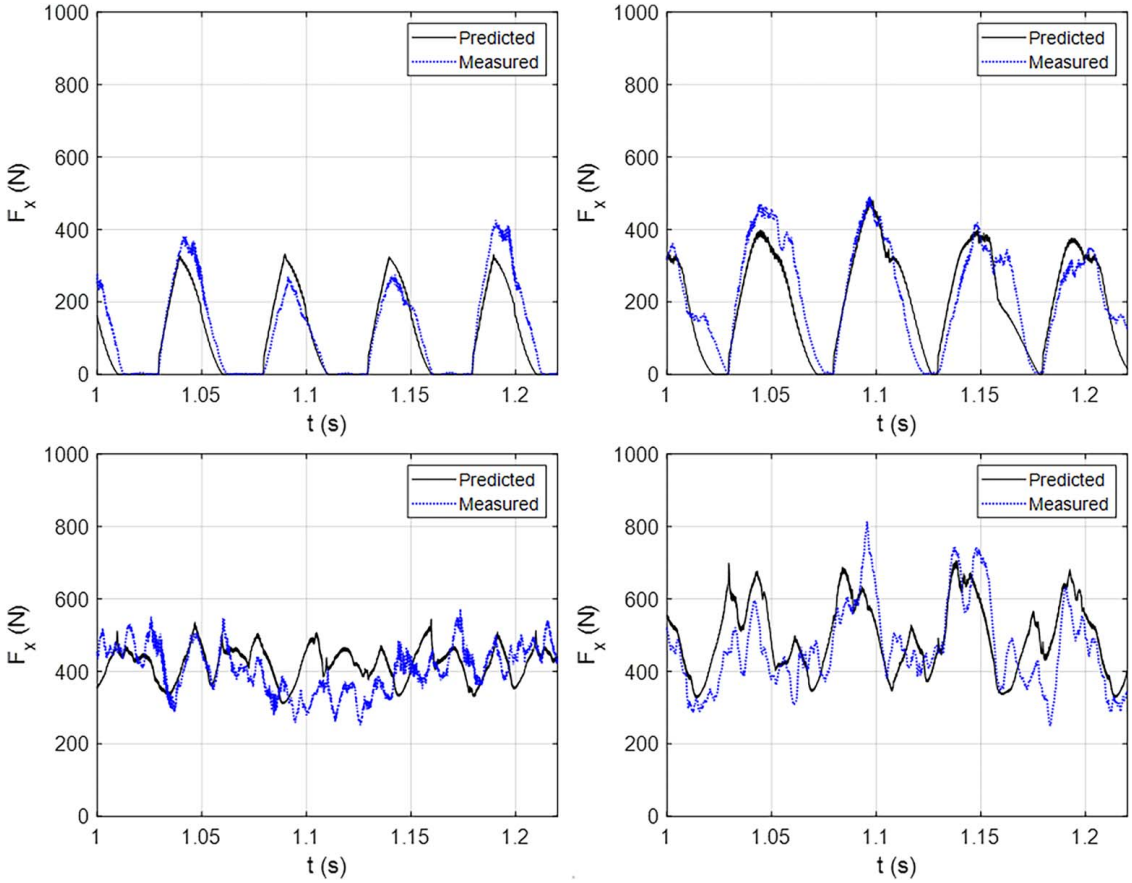

Fig. 23 Measured and predicted force for $b = 5$ mm (top-left), 15 mm (top-right), 20 mm (bottom-left), and 25 mm (bottom-right)

The metric, M, for stable cutting was

$$M = \frac{\sum_{i=2}^{N} |x_s(i) - x_s(i-1)|}{N} \tag{5}$$

where x_s is the vector of sampled x direction displacements and N is the number of samples. To interpret this metric, consider a stable cut where the behavior repeats each revolution and the sampled points are nominally equal. The absolute value of the difference between subsequent points is then zero, and their normalized sum remains zero. If the cut exhibits secondary Hopf bifurcation, on the other hand, the points do not repeat. The difference between subsequent points is then nonzero and, when the sum of the absolute values of these differences is calculated and normalized to the number of points, it is greater than zero. The metric is therefore nominally zero for a stable cut and large for an unstable cut.

Figure 27 displays these binary results, where the single contour represents an M value of 1 μm. This arbitrarily small value was selected because the numerical difference between points, even for a stable cut, is nonzero due to limits on numerical precision. It is observed that there is a stable zone (white area bounded by the

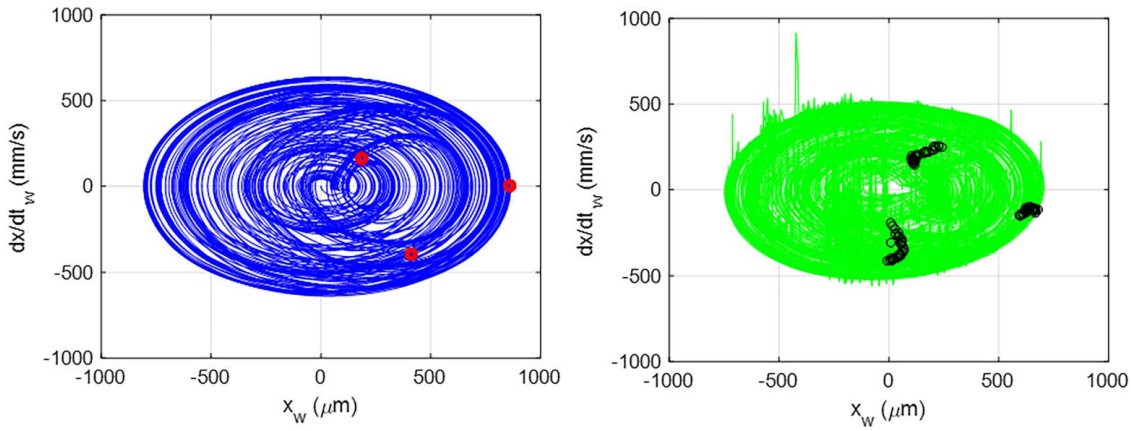

Fig. 24 Poincaré maps for period-3 bifurcation at (2750 rpm, 10 mm): predicted (left) and measured (right). The local jumps in measured velocity are due to chips passing through the laser beam

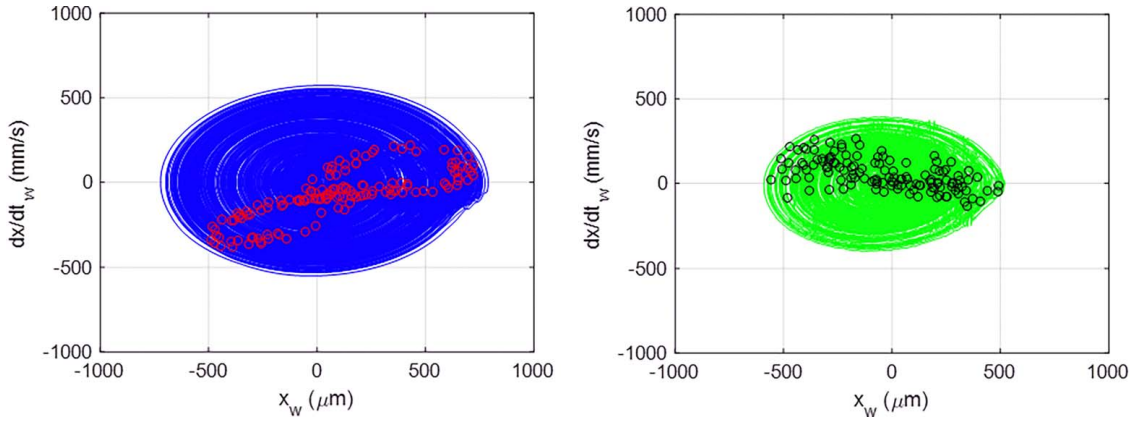

Fig. 25 Poincaré maps for fully developed regenerative chatter (secondary Hopf bifurcation) at 4000 rpm, for 10 mm: predicted (left), note that two ellipses are visible, which departs from the typical secondary Hopf bifurcation sampled point distribution and may be attributed to the non-standard edge geometry for the Walter Tool endmill, and measured (right)

contour where $M < 1\ \mu$m), a complicated stability boundary (at the contour where $M = 1\ \mu$m), and an unstable zone (dark area outside the contour where $M > 1\ \mu$m).

To distinguish between the various bifurcations in the unstable (dark) zone in Fig. 27, subharmonic sampling was implemented [16]. Rather than sampling each revolution, the x direction displacement was sampled in every second revolution to identify spindle speed-axial depth combinations that exhibit period-2 bifurcations. The metric, $M2$, for this case is

$$M2 = \frac{\sum_{i=2}^{N} |x_{s2}(i) - x_{s2}(i-1)|}{N} \tag{6}$$

where x_{s2} is the vector of x direction displacements sampled every second revolution and N is the number of samples. For a period-2 bifurcation, this metric is nominally zero because the displacement repeats every other revolution. As with the M value (Eq. (5)), if the $M2$ value was less than or equal to 1 μm, then a period-2 bifurcation was identified. The same strategy was implemented for higher-order period-n bifurcations, where the sampling interval was n revolutions. Figure 28 shows the corresponding stability map, where period-2 through period-7 bifurcations are separately identified; the symbols are defined in Table 4. Note that if the M value was less than or equal to 1 μm, a black dot was plotted (stable). If M was greater than 1 μm and a period-n bifurcation was not identified by the appropriate metric, then nothing was plotted; the white space in Fig. 28 therefore represents secondary Hopf bifurcations.

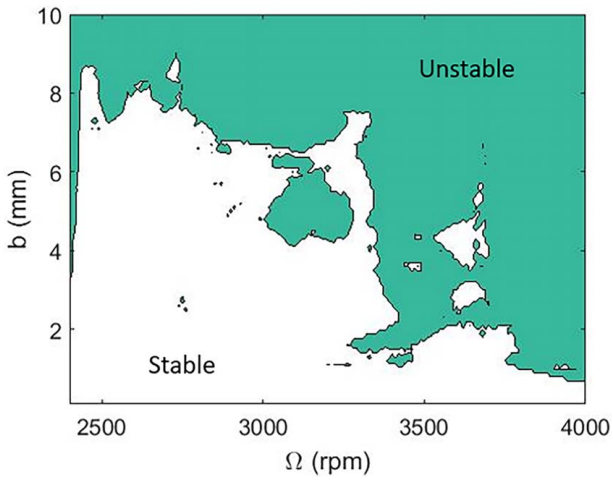

Fig. 27 Stability map for a down milling radial depth of 3 mm and commanded feed per tooth of 100 μm/tooth. The stable and unstable zones are separated by the stability boundary ($M = 1\ \mu$m).

It is now observed that the unstable zone from Fig. 27 is actually a collection of secondary Hopf and period-n cutting conditions. For example, the period-3 behavior displayed in Fig. 24 Poincaré maps at (2750 rpm, 10 mm) is represented as a blue triangle at the corresponding location in the stability map. Overall, the stability

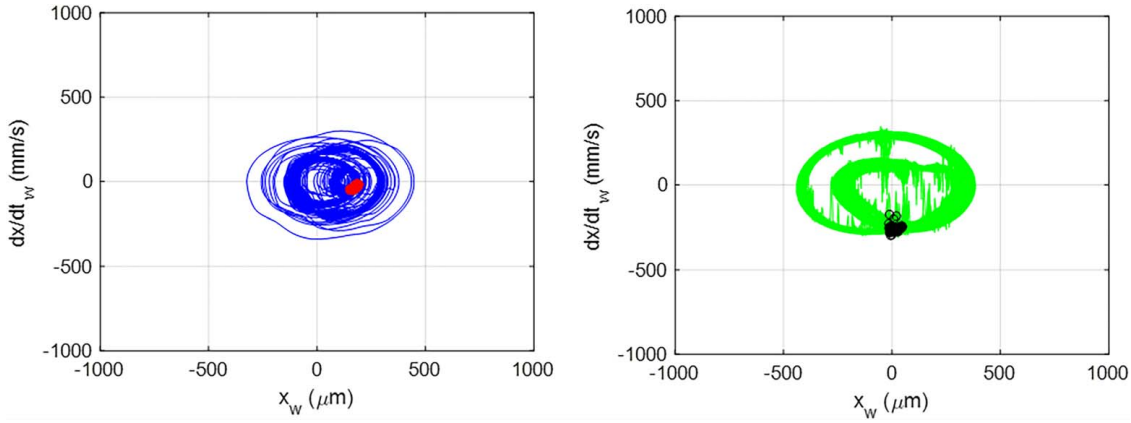

Fig. 26 Poincaré maps for marginally stable cutting at (3400 rpm for 10 mm): predicted (left) and measured (right)

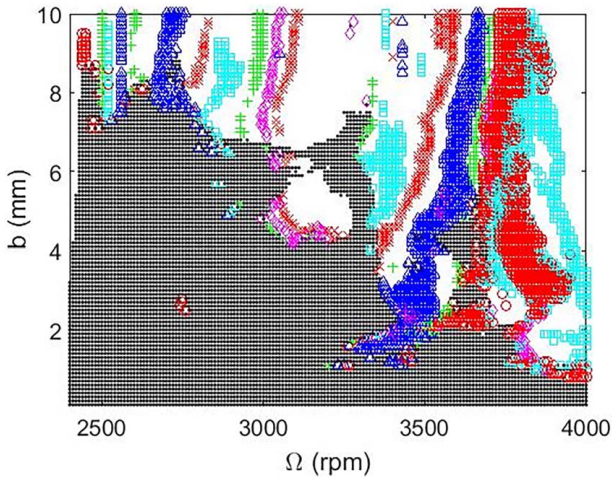

Fig. 28 Stability map for a down milling radial depth of 3 mm and commanded feed per tooth of 100 μm/tooth with bifurcations separately identified by the symbols listed in Table 4

Table 4 Legend for Fig. 28

Symbol	Description
Black dot	Stable
Red circle	Period-2
Blue triangle	Period-3
Cyan square	Period-4
Green +	Period-5
Magenta diamond	Period-6
Red ×	Period-7
No symbol	Secondary Hopf

behavior for the non-standard edge geometry tool significantly departs from the traditional stability boundary. Increased axial depths are available for most spindle speeds.

7 Conclusions

This paper provides a reverse engineering solution for modeling the behavior of non-standard edge geometry endmills. Structured light scanning was used to produce a solid model of two different endmills; this is an important contribution of the effort. From these models, spatial coordinates for the points that define the cutting edges were extracted. The points were used to determine the cutting edge radius and angle at equally spaced points along the tool axis. The cutting edge geometry was then incorporated directly in a time domain simulation that was used to predict cutting force and tool/workpiece deflection for user-selected operating parameters. Variation in the radius of the serrated edge was modeled as runout; this is a second contribution of the paper. A good agreement between predicted and measured cutting forces was obtained.

The simulation was next used to predict stability via a period sampling strategy. Poincaré maps were produced using both the predicted and experimental displacement and velocity signals. Marginally stable, regenerative chatter (secondary Hopf bifurcation), and period-3 bifurcation results were obtained; this also represents a key contribution. Again, a good agreement between prediction and measurement was observed for the non-standard edge geometry endmill. Finally, a stability map was generated to observe the process behavior over a range of spindle speeds and axial depths of cut. Subharmonic sampling was employed to separately identify the different bifurcation types (secondary Hopf and period-n).

Acknowledgment

The authors gratefully acknowledge financial support from MAI BA-21 (USAF contract number FA8650-17-2-5246) and the National Science Foundation (CMMI-1561221; Funder ID: 10.13039/501100008982).

References

[1] Schmitz, T. L., and Smith, K. S., 2009, *Machining Dynamics: Frequency Response to Improved Productivity*, Springer, New York, NY.
[2] Altintas, Y., 2012, *Manufacturing Automation: Metal Cutting Mechanics, Machine Tool Vibrations, and CNC Design*, Cambridge University Press, Cambridge.
[3] Altintas, Y., and Weck, M., 2004, "Chatter Stability of Metal Cutting and Grinding," CIRP Ann. Manuf. Technol., **53**(2), pp. 619–642.
[4] Wang, J.-J., and Yang, C. S., 2003, "Angle and Frequency Force Models for a Roughing End Mill With a Sinusoidal Edge Profile," Int. J. Mach. Tools Manuf., **43**(14), pp. 1509–1520.
[5] Merdol, S. D., and Altintas, Y., 2004, "Mechanics and Dynamics of Serrated Cylindrical and Tapered End Mills," ASME J. Manuf. Sci. Eng., **126**(2), pp. 317–326.
[6] Dombovari, Z., Altintas, Y., and Stepan, G., 2010, "The Effect of Serration on Mechanics and Stability of Milling Cutters," Int. J. Mach. Tools Manuf., **50**(6), pp. 511–520.
[7] Dombovari, Z., Munoa, J., and Stepan, G., 2012, "General Milling Stability Model for Cylindrical Tools," Procedia CIRP, **4**, pp. 90–97.
[8] Stepan, G., Munoa, J., Insperger, T., Surico, M., Bachrathy, D., and Dombovari, Z., 2014, "Cylindrical Milling Tools: Comparative Real Case Study for Process Stability," CIRP Ann. Manuf. Technol., **63**(1), pp. 385–388.
[9] Koca, R., and Budak, E., 2013, "Optimization of Serrated Mills for Reduced Cutting Energy and Higher Stability," Procedia CIRP, **8**, pp. 570–575.
[10] Grabowski, R., Denkena, B., and Köhler, J., 2014, "Prediction of Process Forces and Stability of end Mills With Complex Geometries," Procedia CIRP, **14**, pp. 119–124.
[11] Tehranizadeh, F., and Budak, E., 2017, "Design of Serrated end Mills for Improved Productivity," Procedia CIRP, **58**, pp. 493–498.
[12] Comak, A., and Budak, E., 2017, "Modeling Dynamics and Stability of Variable Pitch and Helix Milling Tools for Development of a Design Method to Maximize Chatter Stability," Precis. Eng., **47**, pp. 459–468.
[13] Munoa, J., Beudaert, X., Dombovari, Z., Altintas, Y., Budak, E., Brecher, C., and Stepan, G., 2016, "Chatter Suppression Techniques in Metal Cutting," CIRP Ann., **65**(2), pp. 785–808.
[14] Smith, K. S., and Tlusty, J., 1991, "An Overview of Modeling and Simulation of the Milling Process," ASME J. Eng. Ind., **113**(2), pp. 169–175.
[15] Honeycutt, A., and Schmitz, T., 2016, "A New Metric for Automated Stability Identification in Time Domain Milling Simulation," ASME J. Manuf. Sci. Eng., **138**(7), p. 074501.
[16] Honeycutt, A., and Schmitz, T., 2017, "Milling Stability Interrogation by Subharmonic Sampling," ASME J. Manuf. Sci. Eng., **139**(4), p. 041009.